A natural variation-based screen in mouse cells reveals USF2 as a regulator of the DNA damage response and cellular senescence

Taekyu Kang[1,2], Emily C. Moore[3], Emily C. K. Kapania[3], Christina D. King[1], Birgit Schilling[1], Judith Campisi[1], Jeffrey M. Good[3], and Rachel B. Brem[1,2*]

[1]Buck Institute for Research on Aging, Novato, CA; [2]Department of Plant and Microbial Biology, UC Berkeley, Berkeley, CA; [3]Division of Biological Sciences, University of Montana, Missoula, MT

*Correspondence: rbrem@berkeley.edu

Abstract

Cellular senescence is a program of cell cycle arrest, apoptosis resistance, and cytokine release induced by stress exposure in mammalian cells. Landmark studies in laboratory mice have characterized a number of master senescence regulators, including $p16^{INK4a}$, p21, NF-kB, p53, and C/EBPβ. To discover other molecular players in senescence, we developed a screening approach to harness the evolutionary divergence between mouse species. We found that primary cells from the Mediterranean mouse *Mus spretus,* when treated with DNA damage to induce senescence, produced less cytokine and had less-active lysosomes than cells from laboratory *M. musculus.* We used allele-specific expression profiling to catalog senescence-dependent *cis*-regulatory variation between the species at thousands of genes. We then tested for correlation between these expression changes and interspecies sequence variants in the binding sites of transcription factors. Among the emergent candidate senescence regulators, we chose a little-studied cell cycle factor, USF2, for molecular validation. In acute irradiation experiments, cells lacking USF2 exhibited compromised DNA damage repair and response. Longer-term senescent cultures without USF2 mounted an exaggerated senescence regulatory program—shutting down cell cycle and DNA repair pathways, and turning up cytokine expression, more avidly than wild-type. We interpret these findings under a model of pro-repair, anti-senescence regulatory function by USF2. Our study affords new insights into the mechanisms by which cells commit to senescence, and serves as a validated proof of concept for natural variation-based regulator screens.

Introduction

Mammalian cells of many types, upon exposure to stress, can enter a senescence program, in which they stop dividing, become refractory to apoptosis, and release soluble inflammation and tissue remodeling factors termed the senescence-associated secretory phenotype (SASP) (Hayflick 1965; Campisi 2005; Campisi and Fagagna 2007; Coppé et al. 2008). The resulting acute immune response can clear debris, promote wound healing, and/or suppress tumorigenesis (Wan et al. 2021; Paramos-de-Carvalho et al. 2021; Baker et al. 2011; Demaria et al. 2014). However, during aging, senescent cells can remain long past any initial triggering event, resulting in chronic inflammation that damages the surrounding tissue (Wan et al. 2021; Olivieri et al. 2018; Davalos et al. 2010; Krtolica et al. 2001; Parrinello et al. 2005). Landmark work has revealed the benefits of eliminating senescent cells to treat age-related pathologies and boost median lifespan (Baker et al. 2011; Demaria et al. 2014; Kang 2019; Kim and Kim 2019).

Establishment of the senescent state and the activity of senescent cells hinge in large part on gene regulatory events. Finding molecular players that control this process is an active area of research. Now-classic work has implicated $p16^{INK4a}$ and p21 in the repression of pro-cell cycle genes and promotion of growth arrest (Campisi 2013) after DNA damage, and NF-kB, p53, and C/EBPβ (Salotti and Johnson 2019) as regulators of the SASP. However, given the complexity of the senescence program, many more regulators likely remain to be identified. Indeed, bioinformatic approaches have identified dozens of other transcription factor candidates (Chan et al. 2022; Wang et al. 2016; Xie et al. 2014; Han et al. 2018; Martínez-Zamudio et al. 2020; Brückmann et al. 2019; Tyler et al. 2021; Zhang et al. 2021), many of which remain unvalidated

(but see (Wang et al. 2016; Xie et al. 2014; Han et al. 2018; Martínez-Zamudio et al. 2020) for recent discoveries of the roles of DLX2, FOXO3 and AP-1 in senescence).

We set out to develop a novel approach to survey transcription factors that play a role in cellular senescence, with the potential for increased specificity relative to traditional genomic screens. Our strategy took advantage of the natural genetic variation in senescence gene expression, and transcription factor binding sites, across mouse species. Among the top hits from this analysis, we chose the under-studied factor USF2 for validation experiments, focusing on gene regulation and cellular phenotypes during senescence induction and maintenance.

Results

A dampened senescence program in primary fibroblasts of *Mus spretus*

We initiated our study on the premise that senescent phenotypes could differ among mouse lineages, and that these changes could serve as a tool to uncover novel regulators. Toward this end, we first characterized the dependence of senescent phenotypes on genotype. We isolated primary tail fibroblasts from PWK, a wild-derived purebred strain of *Mus musculus,* and from the wild-derived, purebred STF strain of the Mediterranean mouse species *M. spretus*. We treated each with ionizing radiation, incubated to allow development of senescence (Campisi and Fagagna 2007; Casella et al. 2019; Zhao and Darzynkiewicz 2013), and assessed features of the resulting senescent cells, with untreated cells as controls. Such cultures from both species arrested growth and exhibited a flattened and enlarged morphology (Figure 1A), as expected if both cultures had entered the senescent state (Zhao and Darzynkiewicz 2013). By contrast, assays of senescence-associated β-galactosidase activity, a senescence biomarker (Dimri et al.

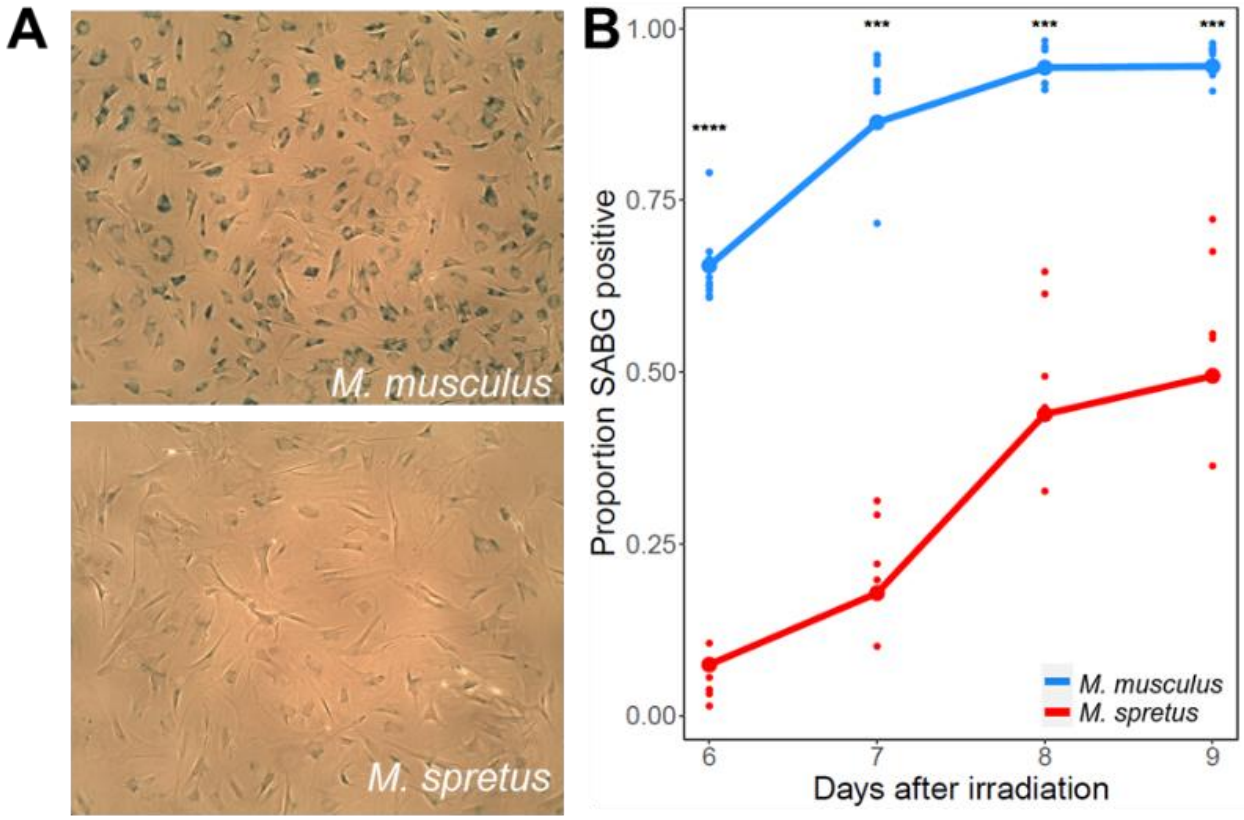

Figure 1: Senescent *M. spretus* cells exhibit lower β-galactosidase activity. (A) Representative images of senescent primary fibroblasts from *M. musculus* (above) and *M. spretus* (below) stained with the β-galactosidase indicator X-Gal seven days after irradiation. (B) Each trace reports results from a timecourse of X-Gal staining assays of primary senescent cells of the indicated species as in (A). The *y*-axis reports the proportion of cells stained positive for senescence-associated β-galactosidase (SABG) activity. In a given column, small points report biological and technical replicates and large points report their average (*M. musculus* $n = 9$, *M. spretus* $n = 5$). ***, $p < 0.001$, ****, $p < 0.0001$, one-tailed Wilcoxon test comparing species.

1995), revealed a marked difference between the cultures, with two to eight-fold lower staining in *M. spretus* cells relative to *M. musculus* cells (Figure 1B).

To explore further the divergence in senescent phenotypes between cells of our focal species, we profiled bulk RNA levels in senescent and control primary fibroblast cultures from each species (Supplemental Table S1). We inspected genes of the SASP immune-stimulatory program (Coppé et al. 2008), and found that this gene cohort was induced more highly in *M. musculus* cells than in those of *M. spretus* during senescence (Figure 2A). Likewise, in an

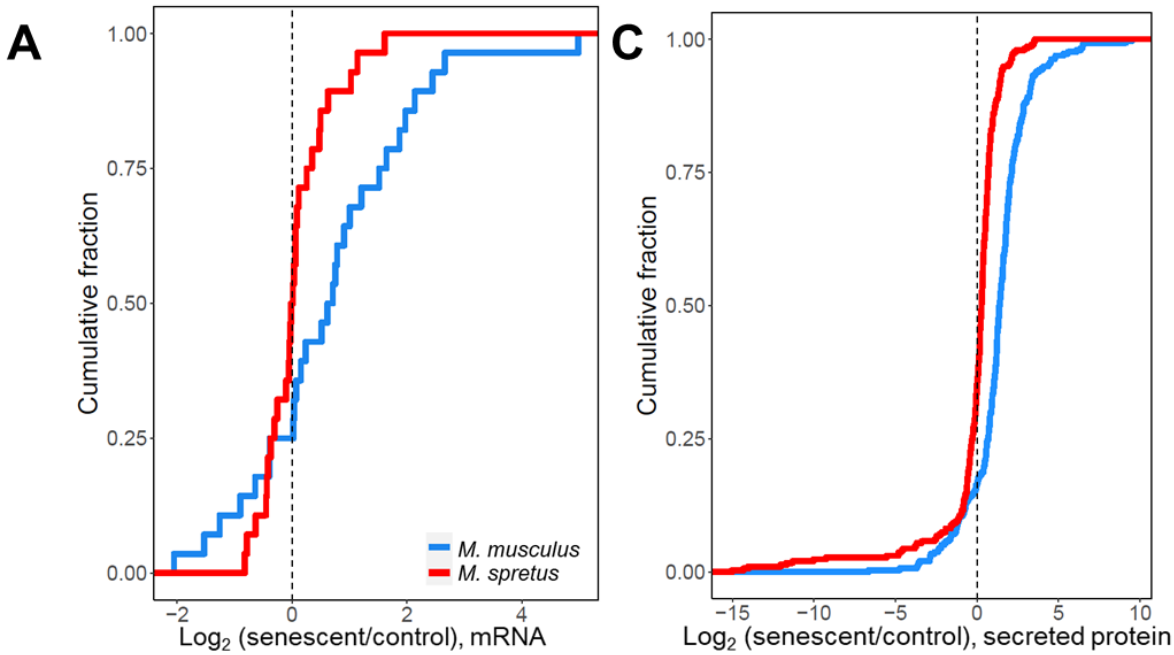

B

GO term	*M. mus* / *M. spr* effect size	p-value	SEN direction in *M. mus* | *M. spr*
antimicrobial humoral immune response mediated by antimicrobial peptide	0.7051633	0.000000	+ | +
regulation of NIK/NF-kappaB signaling	0.3395436	0.000000	+ | -
immune response	0.7865077	0.000000	+ | +
neutrophil chemotaxis	0.4491496	0.018600	+ | +

Figure 2: Senescent *M. spretus* cells express fewer secreted factors. (A) Each trace reports a cumulative distribution of the change, in senescent primary fibroblasts of the indicated species, in mRNA levels of genes of the senescence associated secretory phenotype (Coppé et al. 2008) with senescence. The *y*-axis reports the proportion of genes with the expression change on the *x*-axis, with the latter taken as an average across replicates. (B) Each row shows results from a test of the genes of the indicated Gene Ontology term for enrichment of expression change between the species during senescence, with *p*-values from a resampling-based test, corrected for multiple testing. (C) Annotations are as in (A) except that measurements were of secreted peptides, and the complete set of peptides with significant differential abundance between species is shown.

unbiased search of Gene Ontology terms, we identified several suites of immune response and NF-κB signaling genes that were enriched for senescence-specific differential expression between the cultures. In each case, the gene groups were more strongly induced during senescence in *M. musculus* cells than in *M. spretus* cultures (Figure 2B and Supplemental

Tables S2 and S3); among members of the latter we noted *Cxcl1* (Kim et al. 2018), *Il6* (Coppé et al. 2010b), *Ccls* 2,7 and 8 (Coppé et al. 2010a), *Mmp13* (Levi et al. 2020), and other reported SASP genes (Supplemental Figure S1). These data make clear that, at the level of mRNA, the senescence regulatory program differs markedly between fibroblasts of our focal species.

We hypothesized that much of the divergence between *M. musculus* and *M. spretus* cells during senescence, which we detected in RNA measurements, would result in differential protein abundance. In pursuing this notion, we focused on proteins secreted into the medium by senescent cells, owing to the physiological importance of the SASP (Coppé et al. 2010a). We collected conditioned media from senescent and control cultures of primary fibroblasts of each genotype, and we used it as input into unbiased mass spectrometry to quantify protein abundance. The results revealed an overall increase in the secretion of common SASP components, including CCL chemokines, matrix metalloproteases, and serpins, in senescent *M. musculus* cells relative to those of *M. spretus* (Figure 2C, Supplemental Figure S2, and Supplemental Table S4). Together, our characterization experiments show that *M. spretus* fibroblasts enter a senescent growth arrest similar to that of *M. musculus* fibroblasts, but with expression of certain SASP factors spiking less highly.

A genomic screen for senescence transcription factors using *cis*-regulatory sequence variations

Having established divergence between *M. musculus* and *M. spretus* primary fibroblasts in senescence mRNA and protein secretion (Figures 1 and 2), we reasoned that such differences could be harnessed in an *in silico* screen for senescence regulators. We designed an analysis focused on gene regulation—in particular, on variation between the species at the binding sites

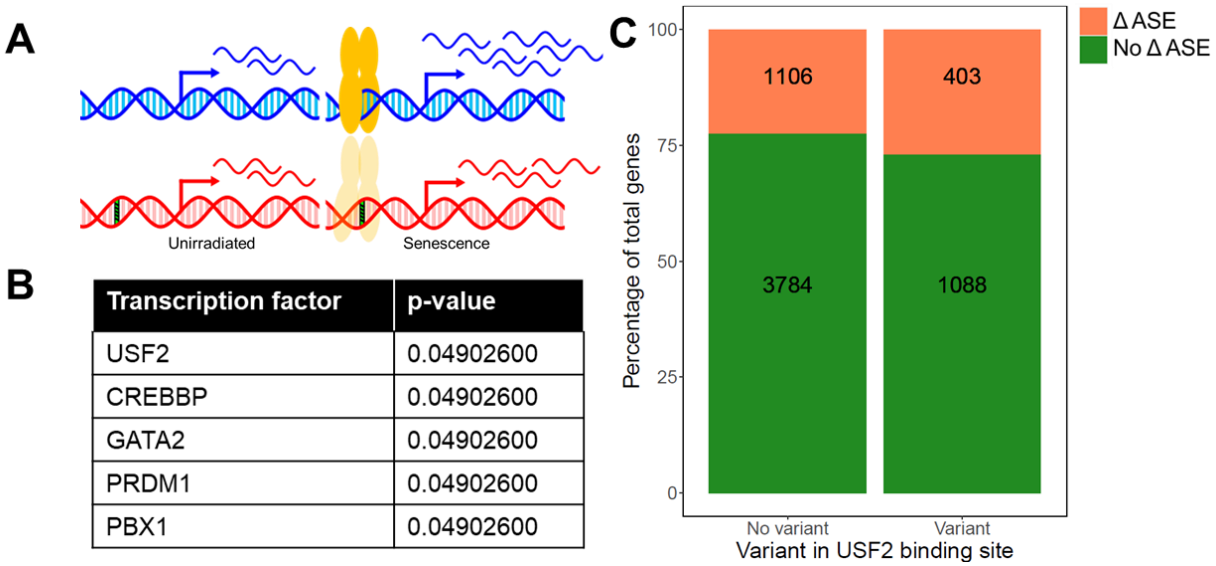

B

Transcription factor	p-value
USF2	0.04902600
CREBBP	0.04902600
GATA2	0.04902600
PRDM1	0.04902600
PBX1	0.04902600

Figure 3: A screen correlating divergence in transcription factor binding sites and *cis*-regulatory expression during senescence reveals USF2 as a top hit. (A) *M. musculus* (blue) and *M. spretus* (red) alleles of a gene are expressed differently in interspecific F1 hybrid cells in a senescence-dependent manner, as a product of a sequence variant (green striped) in the binding site for a transcription factor (yellow). (B) Each row reports the multiple testing-corrected *p*-value from a Fisher's Exact Test of target genes of the indicated transcription factor, quantifying association between species differences in experimentally determined binding sites (Yevshin et al. 2019) and allele-specific expression in primary cells of the *M. musculus* x *M. spretus* F1 hybrid background before and after senescence induction. (C) Shown are the input data for the Fisher's Exact Test in (B) for USF2. Each bar reports analysis of genes with USF2 binding sites in their upstream regions that do (right) or do not (left) harbor sequence variants between *M. musculus* and *M. spretus*. For a given bar, genes are categorized by the presence or absence of senescence-dependent differential allele-specific expression (Δ ASE).

of transcription factors (Figure 3A). We expected that, at some genes, *cis*-regulatory elements encoded in the *M. musculus* genome would drive expression during senescence differently than those in the *M. spretus* genome. We reasoned that if *cis*-acting variation effects were enriched among the loci bound by a given transcription factor across the genome, the signal could be interpreted as a signpost for the factor's activity during senescence (Figure 3A). In this way, all *cis*-regulatory variants between the species that manifested in cultured primary fibroblasts, whether of large or small effect size, and regardless of their potential for phenotypic impact, could contribute to the search for transcription factors relevant for senescence.

As a resource for this approach, we mated PWK *M. musculus* and STF *M. spretus* to yield F1 hybrid animals from which we derived primary tail fibroblasts for culture and irradiation. These *M. musculus* x *M. spretus* F1 hybrid fibroblasts, when irradiated, exhibited a flattened morphology reflecting entry into senescence; senescence-associated β-galactosidase activity was of a magnitude between those of purebred *M. musculus* and *M. spretus* fibroblasts upon irradiation (Supplemental Figure S3). We subjected senescent and control F1 hybrid fibroblasts to RNA-seq profiling, and used the results to quantify levels of transcripts derived from the *M. musculus* and *M. spretus* alleles of each gene in each condition (Supplemental Table S1). At a given gene, any difference between allele-specific expression in an F1 hybrid can be attributed to variants inherited from the parent species that perturb gene regulation in *cis* at the locus, because *trans*-acting factors impinge to the same extent on both alleles (Sun and Hu 2013). Analyzing the response to senescence induction for a given gene, we found that the allele-specific expression difference between the alleles in the F1 hybrid was a partial predictor of the expression divergence between the *M. musculus* and *M. spretus* purebreds, in our primary cell system (Supplemental Figure S4). The latter trend reflects the joint contributions of *cis*- and *trans*-acting variants to total expression divergence between the species, as expected (Wittkopp et al. 2004). Separately, to survey overall regulatory programs in F1 hybrid primary fibroblasts, we formulated the expression level of a given gene in a given condition as the sum of the measured levels of the *M. musculus* and *M. spretus* alleles. In this analysis, focusing on SASP genes as we had done for the purebreds (Figure 2A), we found that the expression program of senescent F1 hybrid cells was, for most genes, intermediate between the low levels seen in *M. spretus* cells and the high levels in *M. musculus* (Supplemental Figure S5). These data indicate that *M. musculus* x *M. spretus* F1 hybrid fibroblasts do not exhibit heterosis with respect to senescence-associated genes, and do manifest extensive, senescence-dependent *cis*-regulatory variation.

We next used the expression measurements from F1 hybrid cells as input into our *in silico* screen to identify senescence-dependent transcription factor activity. For a given transcription factor, we collated binding sites detected by chromatin immunoprecipitation upstream of genes across a panel of tissues (Yevshin et al. 2019). At each site, we tabulated the presence or absence of DNA sequence variants in the respective genomes of *M. musculus* and *M. spretus*. We then tested whether, across the genome, genes with these binding site variants were enriched for senescence-associated expression differences between the two alleles in the F1 hybrid. This test had the capacity for high power to detect even subtle contributions from transcription factors if they had deep binding-site coverage in the input data; five factors attained genome-wide significance (Figure 3B). Among them, PBX1 (Wang et al. 2021) and CREBBP (Bandyopadhyay et al. 2002; Yang et al. 2021) were previously implicated in cellular senescence, providing a first line of evidence for the strength of our approach to identify signatures of condition-dependent transcription factor function. The top-scoring transcription factor in our screen, a basic-helix-loop-helix leucine-zipper protein called upstream stimulatory factor 2 (USF2; Figure 3B-C), had not been experimentally characterized in stress response or senescence. However, classic studies had established USF2 as a regulator of the cell cycle and tumor suppression (Qyang et al. 1999; Pawar et al. 2004; Chen et al. 2006; Aperlo et al. 1996). More recently, USF2 was shown to control cytokine release in immune cells (Hu et al. 2020). Considering these known functions, and bioinformatic analyses suggesting a link between USF2 and senescence programs (Martínez-Zamudio et al. 2020), we chose USF2 for in-depth validation experiments.

USF2 modulates cell proliferation and the acute DNA damage response

Our question at this point was whether and how USF2 regulated senescence programs. As such, we shifted our focus from natural genetic variation to controlled, laboratory-induced

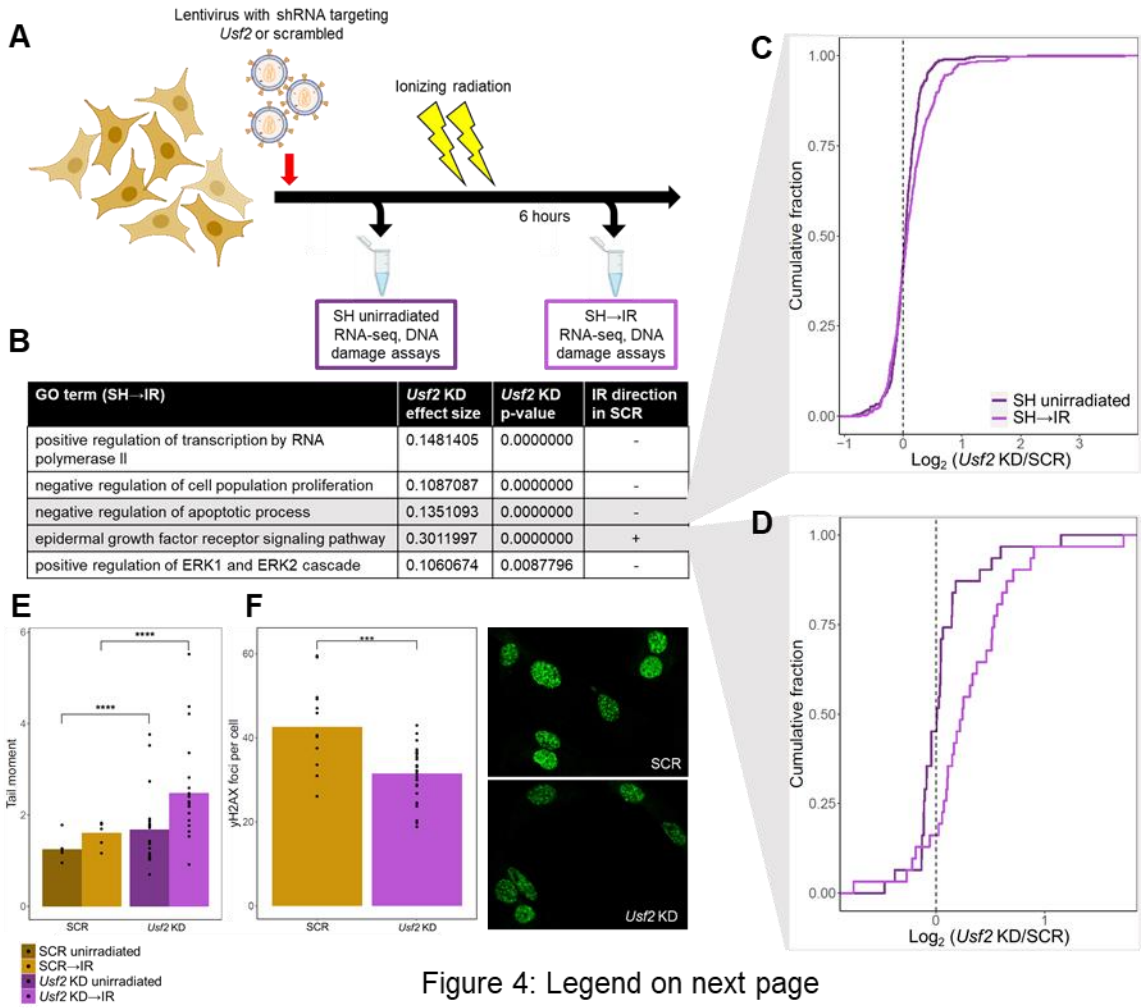

GO term (SH→IR)	*Usf2* KD effect size	*Usf2* KD p-value	IR direction in SCR
positive regulation of transcription by RNA polymerase II	0.1481405	0.0000000	-
negative regulation of cell population proliferation	0.1087087	0.0000000	-
negative regulation of apoptotic process	0.1351093	0.0000000	-
epidermal growth factor receptor signaling pathway	0.3011997	0.0000000	+
positive regulation of ERK1 and ERK2 cascade	0.1060674	0.0087796	-

Figure 4: Legend on next page

genetic perturbations in a single genetic background. We designed two short hairpin RNAs (shRNAs) targeting *Usf2*, each in a lentiviral vector under the U6 promoter. Expression measurements upon transformation of PWK *M. musculus* primary tail fibroblasts confirmed 2.5 and 3-fold knockdown of *Usf2* expression, respectively, from these shRNAs (Supplemental Figure S6). We developed two experimental workflows using these shRNAs. One approach aimed to define the role of USF2 in the acute DNA damage response (Figure 4A) and establishment of senescence (Figure 5A): we infected cells with *Usf2* shRNAs, cultured them under standard conditions, and then induced senescence by irradiation. In a second approach, we focused on the function of USF2 in maintenance of senescence, inducing senescence in wild-type cells and knocking down *Usf2* afterward (Figure 5C).

Figure 4: *Usf2* depletion results in more DNA damage but a muted DNA damage response following irradiation. (A) *M. musculus* primary fibroblasts were infected with a lentivirus encoding a short hairpin RNA (shRNA, SH) targeting *Usf2* or a scrambled control, and analyzed before (SH unirradiated) or six hours after (SH→IR) treatment with ionizing radiation. (B) In a given row, the second column reports the average, across genes of the indicated Gene Ontology term, of the $\log_2$ of the ratio of expression between cells bearing shRNAs targeting *Usf2* and those with a scrambled control (SCR), six hours after irradiation. The third column reports significance in a resampling-based test for enrichment of directional differential expression between *Usf2* knockdown cells and the scrambled control in the respective term, corrected for multiple testing. The fourth column reports the direction of the change in expression before and six hours after irradiation in cells of the scrambled control genotype. (C) Each trace reports a cumulative distribution of the $\log_2$ of the ratio of expression between cells harboring bearing shRNAs targeting *Usf2* or the scrambled control in genes annotated in apoptosis, before or six hours after irradiation treatment as indicated. The *y*-axis reports the proportion of genes with the expression change on the *x*-axis. (D) Data are as in (C), except that EGFR signaling pathway genes were analyzed. (E) Each column reports tail moments detected in a comet assay on primary fibroblasts harboring the indicated shRNAs, before or six hours after irradiation as indicated. In a given column, points report biological and technical replicates and the bar height reports their average (SCR $n = 5$, *Usf2* KD $n = 20$). ****, $p < 0.0001$, one-tailed Wilcoxon test. (F) Left, each column reports number of γH2AX foci per cell detected in primary fibroblasts harboring the indicated shRNAs six hours after irradiation. In a given column, points report biological and technical replicates and the bar height reports their average (SCR $n = 12$, *Usf2* KD $n = 28$). ***, $p < 0.001$, one-tailed Wilcoxon test. Right, representative images of the indicated cultures.

Given that our first experimental design used *Usf2* knockdown in cells under standard conditions to study the irradiation response and senescence (Figures 4A and 5A), we began by characterizing the effects of reduced *Usf2* expression in resting cells. Uptake of the nucleotide analog EdU, a marker of DNA synthesis, was reduced by 40% in resting primary fibroblasts expressing the *Usf2* shRNA relative to scrambled shRNA controls (Supplemental Figure S7). Transcriptional profiling of these resting cultures (Supplemental Table S5), followed by functional-genomic (Gene Ontology) analyses, revealed enrichment for biosynthesis, development, cell growth, and DNA repair terms altered upon *Usf2* knockdown relative to controls (Supplemental Table S6). These data support a role for USF2 in wild-type growth and housekeeping gene expression programs in untreated primary fibroblasts, consistent with studies of USF2 in cell growth in other tissues and contexts (Zhao and Darzynkiewicz 2013; Qyang et al. 1999; Pawar et al. 2004; Chen et al. 2006; Aperlo et al. 1996). Our results in

resting cells also provide a first indication of the potential function of USF2 in DNA damage response.

We next directly pursued the importance of USF2 during the acute response to irradiation (Figure 4A). DNA damage signaling, an inducer of cellular senescence (Campisi 2005; Campisi and Fagagna 2007), drops sharply in intensity within eight hours and then more gradually over several day after irradiation (Redon et al. 2009), culminating in a lower persistent signal (Fumagalli et al. 2014; Chen and Ozanne 2006; Bakkenist et al. 2004; Siddiqui et al. 2015). We focused on the early phase of this process (six hours after irradiation) in cultures of primary fibroblasts expressing *Usf2* shRNAs or scrambled shRNA controls. Transcriptional profiling followed by Gene Ontology enrichment analyses identified top-scoring gene groups (Figure 4B and Supplemental Tables S5 and S7). Most salient was a trend of pervasive repression transcriptome-wide six hours after irradiation, which was detected in control cells as expected (Venkata Narayanan et al. 2017; Silva and Ideker 2019), and was blunted in cells with *Usf2* knocked down. The latter effect was particularly enriched in the transcriptional machinery, repressors of apoptosis, and several cell proliferation regulators (Figure 4B-C and Supplemental Figure S8A). We also inspected the few top-scoring gene groups that were induced by irradiation in control cultures. These gene groups reached even higher expression levels in *Usf2* knockdown cells; notable among them was the EGFR pathway (Figure 4B and 4D and Supplemental Figure S8B), a determinant of entry into senescence in some contexts (Shang et al. 2020). DNA repair genes, a likely target for changes upon irradiation, are regulated primarily at the post-transcriptional level (Huang and Zhou 2020; Nickoloff et al. 2017), and we did not detect effects of *Usf2* knockdown on their transcripts (Supplemental Figure S9).

We hypothesized that *Usf2* knockdown during the acute DNA damage response would also have cell-physiological effects. Assays of EdU incorporation to report on DNA synthesis

showed effects of *Usf2* knockdown after irradiation to the same degree seen in resting cultures (Supplemental Figure S7). To focus on phenotypes more proximal to DNA damage, we used the neutral comet assay (Olive and Banáth 2006) to measure DNA double-stranded breaks on a per-cell basis. In this setup, *Usf2* depletion increased comet tail moments by 50% six hours after irradiation, with an effect that was similar, though of smaller magnitude, in resting cell controls (Figure 4E). Next, we tracked foci of phosphorylated histone H2AX (γH2AX) in fibroblasts as a marker of chromatin decondensation, preceding the repair of DNA double-stranded breaks (Podhorecka et al. 2010). Cells harboring *Usf2* shRNAs exhibited 30% fewer γH2AX foci than cells of the control genotype, six hours after irradiation (Figure 4F). These data establish a role for USF2 in the response to irradiation, with knockdown of this factor compromising cells' ability to mount the classical transcriptional program under this stress, and to carry out DNA damage repair.

USF2 tunes the commitment to senescence

Having knocked down *Usf2* in naïve PWK primary fibroblasts and irradiated them to study the acute DNA damage response, we now allowed the irradiated cultures to enter senescence (Figure 5A). Growth arrest and flattened morphology were indistinguishable between these cells and controls harboring scrambled shRNAs (see Figure 5G), indicating that wild-type levels of *Usf2* were not required at the point of irradiation to establish senescence *per se*. To investigate quantitative characteristics of these senescent cultures, we subjected them to expression profiling and Gene Ontology enrichment analyses (Supplemental Tables S5 and S8). Among top-scoring gene groups, the most dramatic effects were in those that dropped in expression in senescent cultures of the control genotype, which as expected (Kim et al. 2013b; Chan et al. 2022) included cell cycle and DNA repair pathways (Figure 5B and Supplemental

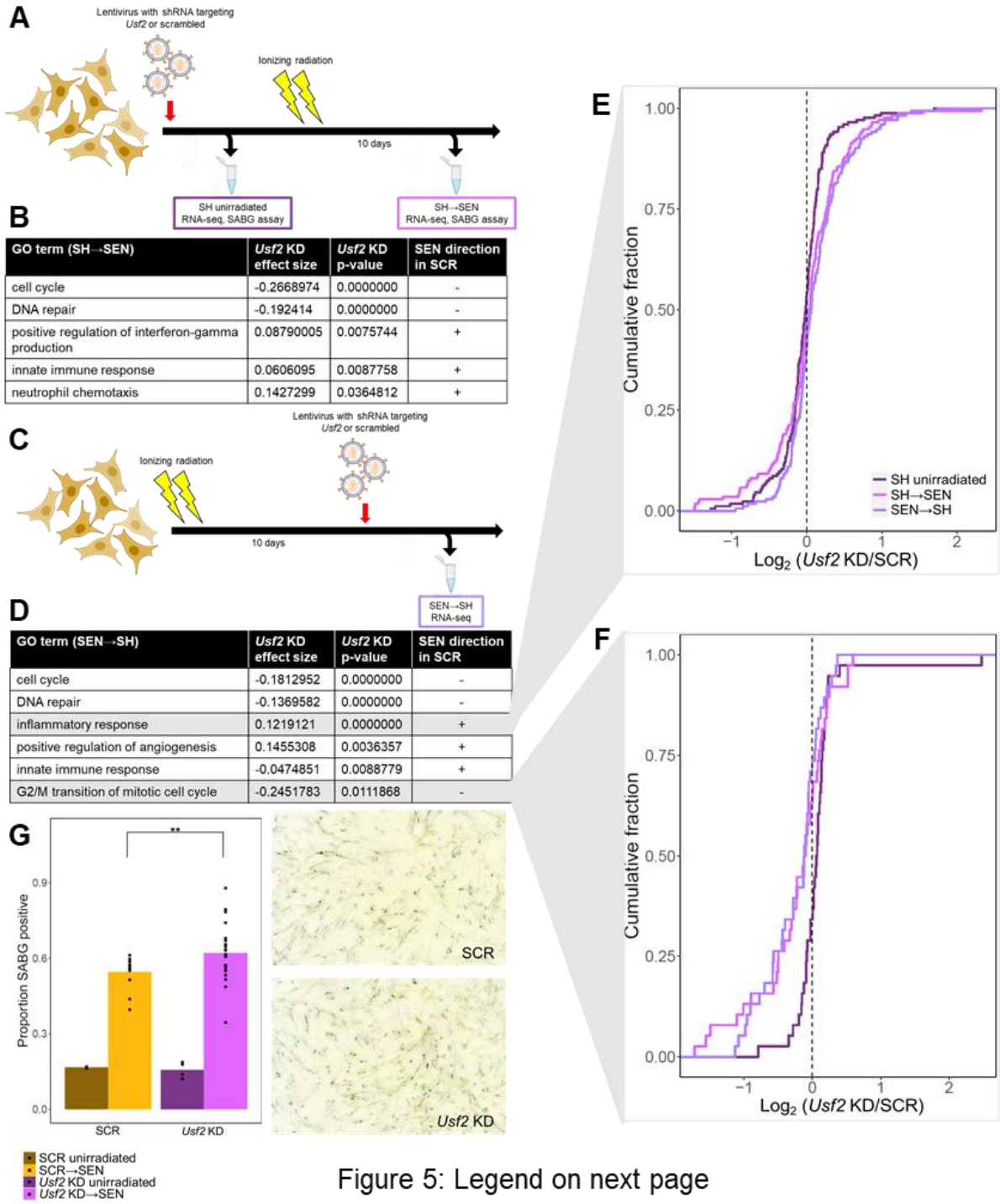

GO term (SH→SEN)	*Usf2* KD effect size	*Usf2* KD p-value	SEN direction in SCR
cell cycle	-0.2668974	0.0000000	-
DNA repair	-0.192414	0.0000000	-
positive regulation of interferon-gamma production	0.08790005	0.0075744	+
innate immune response	0.0606095	0.0087758	+
neutrophil chemotaxis	0.1427299	0.0364812	+

GO term (SEN→SH)	*Usf2* KD effect size	*Usf2* KD p-value	SEN direction in SCR
cell cycle	-0.1812952	0.0000000	-
DNA repair	-0.1369582	0.0000000	-
inflammatory response	0.1219121	0.0000000	+
positive regulation of angiogenesis	0.1455308	0.0036357	+
innate immune response	-0.0474851	0.0088779	+
G2/M transition of mitotic cell cycle	-0.2451783	0.0111868	-

Figure 5: Legend on next page

Table S8). mRNA levels of the latter were even lower in senescent cells that had been irradiated after *Usf2* knockdown, showing a reduction of ~20% on average (Figure 5B). Among the genes of this cohort, some of which declined in expression by >5-fold with *Usf2* knockdown in senescence (Figure 5F), we noted cell cycle regulators (*Ccna2*, *Cdc20*, *Cdk1),* kinesin

Figure 5: *Usf2* knockdown results in an enhanced senescence profile. (A) *M. musculus* primary fibroblasts were infected with a lentivirus encoding an shRNA (SH) targeting *Usf2* or a scrambled control, and analyzed before (SH unirradiated) or after (SH→SEN) treatment with ionizing radiation (IR) to induce senescence (SEN). (B) Data are as in Figure 4B except that cells were analyzed 10 days after irradiation. (C) *M. musculus* primary fibroblasts were irradiated, incubated for 10 days to senesce, then infected with shRNAs and analyzed after 10 additional days. (D) Data are as in (B) except that cells from the scheme in (C) were analyzed. (E) Each trace reports a cumulative distribution of the $\log_2$ of the ratio of expression in cells bearing shRNAs targeting *Usf2* and those with a scrambled control (SCR), in genes annotated in the inflammatory response, when shRNAs were administered to a resting culture (SH unirradiated), to resting cells followed by irradiation (SH→SEN), or after irradiation and senescence establishment (SEN→SH). The *y*-axis reports the proportion of genes with the expression change on the *x*-axis, with the latter taken as an average across replicates. (F) Data are as in (E), except that genes involved in G2/M transition of mitotic cell cycle were analyzed. (G) Left, each column reports the proportion of senescence associated β-galactosidase (SABG) positive cells treated with the indicated shRNAs in resting culture (unirradiated) or 7 days after irradiation (SEN). In a given column, points report biological and technical replicates and the bar height reports their average (unirradiated $n = 4$, SEN $n = 24$). **, $p < 0.01$, one-tailed Wilcoxon test. Right, representative images of the indicated cultures.

components (*Kif2c, Knl1*), the DNA polymerase *Pole,* and the DNA damage checkpoint ubiquitin ligase *Uhrf1* (Supplemental Figure S10A). We conclude that genes of the cell cycle and DNA repair machinery are detectable at a low but non-zero expression level in wild-type senescent cells, and that these pathways are subject to further reduction when *Usf2* is limiting.

Next, we analyzed the impact of *Usf2* knockdown on inflammation and immune recruiting factors. Cells of the control genotype induced these pathways during senescence, as expected (Campisi 2005; Campisi and Fagagna 2007; Olivieri et al. 2018; Coppé et al. 2010b; Santoro et al. 2018; Kale et al. 2020); in cells reaching senescence after *Usf2* knockdown, induction of inflammatory factors was amplified by ~10% on average (Figures 5B and 5E, and Supplemental Figure S10B). Similarly, in assays of the β-galactosidase senescence marker, we observed a modest, though robustly significant, increase in cells subject to *Usf2* knockdown and senescence treatment (Figure 5G). Together, our profiling data establish that irradiation of primary fibroblasts with reduced *Usf2* expression leads to a quantitatively perturbed,

exaggerated senescent state, with reduced expression of proliferation and DNA repair pathways, and elevated pro-inflammatory gene expression and β-galactosidase activity.

We reasoned that the changes in senescence we had seen upon irradiation of *Usf2*-depleted cells could constitute, in part, effects from increased DNA damage in the knockdown genotype (Figure 4). To pursue the role of USF2 in senescence more directly, we used our second experimental paradigm: we irradiated wild-type cells, incubated them for 10 days to allow establishment of senescence, then expressed shRNAs targeting *Usf2,* followed by 10 additional days of incubation and transcriptional profiling (Figure 5C). In control cells (harboring a scrambled shRNA), we observed expression changes for many genes from the resting state through irradiation and early and late senescence (Supplemental Tables S5 and S9, and Supplemental Figure S11), attesting to the dynamics of senescence across this timecourse as expected (Kim et al. 2013b; Chan et al. 2022). Next we focused on cultures subject to *Usf2* knockdown during late senescence. The latter manifested quantitative changes largely paralleling those in cells with *Usf2* knocked down at the start of the experiment. Thus, on average, cell cycle and DNA repair genes, repressed in control cells during senescence, were expressed at even lower levels when *Usf2* was knocked down midway through the senescence time course (Figures 5D and 5F, Supplemental Tables S5 and S10, and Supplemental Figure S10A), analogous to our findings using early knockdown of *Usf2*. Likewise, inflammatory response factors, induced during senescence in the control setting, were more highly expressed when *Usf2* was depleted after senescence establishment, as seen in our early-knockdown design (Figures 5D and 5E, Supplemental Tables S5 and S10, and Supplemental Figure S10B). We noted a handful of genes for which early *Usf2* knockdown effects were not recapitulated in our paradigm of knockdown after senescence entry (*e.g. Adamts1* and *Rarres2* in Supplemental Figure S10B). Overall, however, our analyses establish USF2 as a senescence regulator at

least in part independent of its role in the acute DNA damage response, such that in its absence, cells commit even more strongly to the senescent state.

Discussion

Complex regulatory networks likely underlie many of the quantitative behaviors of senescent cells, including kinetics and dependence on cell type and inducer (Campisi 2013; Chan et al. 2022; Casella et al. 2019; Basisty et al. 2020; Purcell et al. 2014). Exactly how these nuances are encoded remains poorly understood. In this study, we pioneered the use of interspecies genetic divergence to screen for components of the senescence regulatory machinery. This strategy complements previous studies of transcription factor binding sites in genes of the senescence program in a single genetic background (Chan et al. 2022; Martínez-Zamudio et al. 2020). Our approach harnesses the correlation between interspecies variation in sequence and expression levels, as an additional line of evidence for senescence-specific regulatory functions by a given factor. This paradigm parallels similar tools previously used to dissect expression divergence in other contexts (Villarroel et al. 2021; Veyrieras et al. 2008). Broadly speaking, these methods are not highly powered for pathways under strong evolutionary constraint, which, by definition, will not vary enough among species to yield the raw observations that would go into a screening pipeline. Rather, we expect the natural variation-based approach to work best for discovering less-constrained modifiers, many of which may confer layers of quantitative regulation onto a master regulatory pathway.

We focused our experimental validation on one such modifier, the transcription factor USF2. By tracing USF2's function in proliferation and genome-wide expression in untreated cells, we extended conclusions from studies of USF2 in tumor suppression and cell cycle regulation

(Qyang et al. 1999; Pawar et al. 2004; Chen et al. 2006; Hu et al. 2020), apoptosis (Sato et al. 2011) and ERK1/2 signaling (Chi et al. 2020). In an acute DNA damage setting, we discovered that USF2 is required for cells to mount DNA repair and downstream DNA damage responses. And in senescence proper, we showed that USF2 acts as a repressor, such that in its absence, the senescence program—shutoff of cell proliferation and DNA repair, and induction of cytokines—is amplified. A compelling model is thus that even long after damage exposure, cells have access to expression states along a continuum of commitment to senescence, and that USF2 acts to help determine which state they occupy. If so, USF2 would take a place among a network of factors, including p53, ING, Rb (Vicencio et al. 2008; Childs et al. 2014), p21 (Zhang et al. 2005; Hsu et al. 2019), and p16 (Panneer Selvam et al. 2018), that govern the choice between senescence, apoptosis, and repair and proliferation, depending on cell type (Vicencio et al. 2008) and the amount of damage or stress incurred (Childs et al. 2014).

As a corollary of these conclusions from expression profiling, we note that cell cycle and DNA repair genes, classically known to be repressed during senescence (Kim et al. 2013b; Chan et al. 2022), did not hit a floor of expression in senescent cultures: we could detect them at even lower expression levels upon *Usf2* knockdown. Since our cultures comprise >99% arrested cells within several days of irradiation (see Methods), the emerging picture is that the proliferation machinery is maintained at non-zero levels even in such a population. Any ability of these gene products to reattain activity could be of particular interest as a potential mediator of the return to proliferation seen among senescent cells in certain scenarios (Lee and Schmitt 2019; Beauséjour et al. 2003).

Our work leaves open the mechanisms by which USF2 exerts its effects in the DNA damage response and cellular senescence. It is tempting to speculate that USF2 ultimately works in these processes in concert with its better-studied family member, USF1. Indeed, USF1 has

been implicated in DNA repair (Baron et al. 2012), inflammation (Song et al. 2018; Ruuth et al. 2018), immune responses (Corre and Galibert 2005), and p53-mediated cell cycle arrest (Bouafia et al. 2014) in contexts other than senescence. In addition, given that USF2 has been implicated in the TGFβ-p53 axis in apoptosis (Sato et al. 2011) and fibrosis (Samarakoon et al. 2012), the latter pathway could mediate some part of the USF2 effects we have seen. Furthermore, regulatory network reconstruction (Supplemental Table S11) suggests that USF2 acts upstream of several other transcription factors (KLF3, GLI3, NFIL3) with direct targets in DNA repair, DNA damage response and senescence pathways.

Alongside our use of *cis*-regulatory variation between mouse species as a screening tool for senescence genes, we also characterized overall patterns of divergence between *M. spretus* senescent cells and those of *M. musculus*. Given that the former exhibited lower levels of SASP mRNAs and proteins, we suggest that the rheostat of the senescence response is at a higher set point in this species, such that at a given level of stress (*e.g.* the irradiation we study here), cells of this species synthesize and secrete less of the SASP. We further hypothesize that this down-tuning might be a proximal cause for the lower senescence-associated β-galactosidase activity we have seen in *M. spretus* cells. Such a link would follow from current models of the senescent state in which production and secretion of SASP components (Dörr et al. 2013) leads to proteotoxic stress from insoluble aggregates (Park et al. 2018; Brunk and Terman 2002), an increase in the number and size of lysosomes (Kurz et al. 2000), and enhanced β-galactosidase activity (Lee et al. 2006). Plausibly, any of the phenotypes we study here in cell culture could have consequences *in vivo*, with potential links to the stress- and pathogen-resistance phenotypes characterized in *M. spretus* (Pinheiro et al. 2013; Vanlaere et al. 2008; Blanchet et al. 2011; Pérez del Villar et al. 2013; Dejager et al. 2009). Together, our findings attest to the power of natural variation-based-approaches—to survey the differences

that evolution has wrought over long timescales, and as a tool for molecular discoveries of relevance in any one genetic background.

Methods

Primary cell extraction and culture

Wild-derived, inbred lines of *Mus musculus* (PWK/PhJ) and *Mus spretus* (STF/Pas) and their interspecies F1 hybrids (*M. musculus* x *M. spretus*) were maintained in standard conditions under Montana Institutional Animal Care and Use Committee protocol number 062-1JGDBS-120418. Animals aged 3 to 5 months were humanely euthanized prior to tissue collection via CO_2 treatment and cervical dislocation. Five tails from each genotype were collected into chilled Dulbecco's Modified Eagle Medium (DMEM) and shipped to the Buck Institute for further processing. Metadata for the mice used in this experiment is provided in (Supplemental Table S12). Primary tail fibroblasts were extracted from the cuttings essentially as described (Khan and Gasser 2016). Briefly, tail cuttings first were soaked in 70% ethanol for 5 minutes and then laid out in sterile 10 cm tissue culture dishes in a biosafety cabinet for 5 minutes to dry. The tails were then transferred to a 10-cm dish containing 10 mL of complete medium (RPMI 1640 medium, 10% fetal bovine serum, 50 µM 2-mercaptoethanol, 100 µM asparagine, 2 mM glutamine, and 1% penicillin-streptomycin). All hair was removed from the tails using sterile forceps and razor blade, and the tails were cut into 2-3 mm pieces using sterile surgical scissors. These pieces were then transferred into a 2 mL cryotube containing a collagenase D–pronase solution and left in a shaking incubator at 37ºC for 90 minutes. Following incubation, the contents of the cryotubes were placed into a 70 µm cell strainer in a new 10-cm dish containing 10 mL of compete medium. Using the back end of a sterile 10 mL syringe plunger,

the tissue was ground into the strainer for 5-10 minutes to release the cells into the media. The cell suspension was then collected into 15 mL conical tubes and centrifuged at 580 x g and 4ºC for 5 minutes. The supernatant was removed and replaced with fresh complete medium, and the centrifugation was repeated for two additional rounds. After the final spin, the media was replaced with complete medium supplemented with 250 ng/mL of amphotericin B. The cell suspension was placed in a 10-cm dish and incubated in a 37ºC humidified incubator at 3% O_2 and 10% CO_2 for two days before passage and continued culture in complete medium (DMEM, 10% FBS, 1% penicillin-streptomycin). This complete medium was used for the remainder of our experiments. For long term storage, cells were suspended in 5% DMSO in FBS, aliquoted into cryotubes, and placed in a slow cooling container in a -80ºC freezer overnight. The following day, the cryotubes were moved out of the slow cooling container and placed into long term containers in the freezer. To thaw cells for continued culture, cryotubes containing frozen aliquots were swirled in a 37ºC water bath until only a thin layer of ice remained in the vial. The contents of the cryotube were then immediate transferred into a flask containing pre-warmed complete medium and incubated overnight. The following day the cells were washed twice with PBS to remove any trace of DMSO and cultured in complete medium. For experiments in wild-type *M. musculus*, *M. spretus*, and F1 hybrid cells we considered the culture from each individual animal to represent one biological replicate of the respective genotype. In knockdown experiments (see below) we carried out infection of two such cultures with each shRNA-bearing virus, which we refer to as biological replicates. In either setup, we refer to the split cultures from a given biological replicate as technical replicates in a given assay.

Irradiation treatment

To treat a given cell culture replicate with ionizing radiation (Campisi and Fagagna 2007; Casella et al. 2019; Zhao and Darzynkiewicz 2013) for a cell-biological assay or omics profiling,

we proceeded as follows. The day before irradiation, cells were seeded at 60-70% confluency and incubated in a 37ºC humidified incubator at 3% O_2 and 10% CO_2 overnight in complete medium. The next day, a subset of cells was collected and used as input into the respective experiment as the unirradiated control. The remainder of the culture was transferred into an X-RAD 320 X-Ray Biological Irradiator and treated with 15 Gy of X-ray irradiation. Cultures were then placed back into the 37ºC humidified incubator at 3% O_2 and 10% CO_2 until sampling at 6 hours for marker assays and RNA-seq focused on acute DNA damage response, or 7, 10 or 20 days for marker assays and RNA-seq and proteomics focused on senescence (in which case the medium was replaced 6-8 hours after irradiation, then every 48 hours for the remainder of the experiment), as detailed below.

Senescence marker assays

For a given replicate culture after irradiation and incubation (see above), senescence-associated β-galactosidase activity was measured using the BioVision Inc. Senescence Detection Kit (cat. #K320): cells were fixed, permeabilized, and incubated with the staining solution containing X-gal overnight. Multiple images were taken the following day using a brightfield microscope, and the image names were randomized before the proportion of β-galactosidase-positive cells was counted manually to remove potential sources of bias. Cultures were considered to be senescent if they showed less than 10% EdU incorporation (see below) and over 90% β-galactosidase-positive cells. In the species comparison of Figure 1 we subjected two technical replicate cultures of each of three biological replicates per purebred species to irradiation (see above) followed by β-galactosidase assays at the indicated timepoints. In Supplemental Figure S3, data for purebreds were from Figure 1 at day 7; separately, for the interspecies F1 hybrid, we carried out irradiation and β-galactosidase assays

as above for two technical replicates from one biological replicate. In Figure 5G, we carried out irradiation and β-galactosidase assays as above at day 7 after irradiation for two technical replicates from each of two biological replicates of *M. musculus* cells infected with lentivirus harboring the scrambled control and two of each *Usf2* knockdown (see below).

RNA collection and sequencing

For a given replicate culture of a given genotype, either before irradiation or 6 hours, 10 days, or 20 days after irradiation (see above), cells were treated with TRIzol™ and RNA was extracted using chloroform and ethanol precipitation. The RNA was then further purified using the Qiagen RNeasy Kit (cat. #74004) for DNase treatment and column cleanup. The purity of the extracted RNA was verified using a NanoDrop ND-1000 Spectrophotometer; all samples had 260/280 and 260/230 ratios greater than 2.0. Purified RNA in distilled RNase/DNase free water was snap frozen using dry ice and stored at -80ºC. Samples were then either transferred to the QB3 Genomics core at University of California, Berkeley for library prep and sequencing on 150PE NovaSeq S4 or shipped to Novogene Co. (Sacramento, CA) for the same. Both facilities provided 25 million paired end reads per sample. For expression profiles of purebred cells and *M. musculus* x *M. spretus* F1 hybrid cells, we subjected three biological replicates of a given genotype to irradiation (see above) followed by RNA-seq at the indicated timepoints. To assess transcriptional impacts of *Usf2* knockdown we carried out irradiation and RNA isolation as above for two biological replicates of *M. musculus* cells infected with lentivirus harboring the scrambled control and two of each *Usf2* knockdown (see below).

Pseudogenome and VCF generation

As publicly available annotations for *M. musculus* and *M. spretus* are in the context of their reference genomes (GRCm38.96 and SPRET_EiJ_v1.96 respectively), custom pseudogenomes for strains PWK and STF were generated and used for this study. For the PWK pseudogenome, variant calls between PWK and the reference genome in the form of a variant call file (VCF) were downloaded from the Sanger Mouse Genomes Project database (https://www.sanger.ac.uk/data/mouse-genomes-project/). A pseudogenome using the VCF and the GRCm38.96 reference genome was created using bcftools v1.9 (Danecek et al. 2021). To generate shotgun sequence data for the STF pseudogenome, DNA was extracted from *M. spretus* liver tissue using Qiagen DNeasy spin columns (cat. #69506). The sample was sheared via sonication (Covaris E220), and prepared using the New England Biolabs NEBNext Ultra DNA Library kit (cat. #E7370L). The final library was sequenced on a single lane of 150bp PE Illumina HiSeq X at Novogene, Inc. The latter reads were aligned to the SPRET_EiJ_v1.96 reference genome using bowtie v2.2.3 (Langmead and Salzberg 2012), and a VCF was generated using bfctools mpileup and filtered for quality, depth, and SNPs using vcfutils (Li et al. 2009; Li 2011). The VCF was then used with the reference genome to create a STF pseudogenome using bcftools. The pseudogenomes were verified by identifying a number of called variants by hand. A VCF of variants between the STF and PWK pseudogenomes was generated as above aligning the STF whole genome sequencing reads to the PWK pseudogenome.

RNA-seq processing

In transcriptional profiles of *M. musculus* x *M. spretus* F1 hybrid cells, sequencing reads from a given replicate were aligned to a concatenated PWK/STF pseudogenome using tophat v2.1.1 (Kim et al. 2013a) allowing for zero mismatches to ensure allele specific mapping. Alignments were then filtered for uniquely mapped reads using samtools v1.3.1, and gene counts were

generated using HTSeq v0.11.2 (Putri et al. 2022) and genome annotations (GRCm38.96, SPRET_EiJ_v1.96) for both species from Ensembl. Counts were then converted to transcripts per million (TPM) using custom R scripts, and genes were filtered for those showing counts in more than half the samples sequenced.

In transcriptional profiles of purebred *M. musculus* wild-type cells and *M. musculus* cells infected with lentiviruses harboring shRNAs, RNA-seq processing was as above but mapping was to the PWK pseudogenome only; for profiles of purebred *M. spretus* wild-type cells, mapping was to the STF pseudogenome only.

Data for the average TPM across biological replicates for purebred parents and interspecific F1 hybrid are available in (Supplemental Table S1). Average TPM across biological replicates for shRNA treated *M. musculus* cells in each condition is available in (Supplemental Table S5).

Gene Ontology enrichment analysis of RNA-seq data

For the comparison of transcriptional profiles of *M. musculus* and *M. spretus* purebred cells, for each gene in turn we tabulated the average TPM count from each species across replicates, and then took the $\log_2$ of the ratio of these averages, $r_{sen,true}$. We downloaded Gene Ontology annotations from the AmiGO 2 (Ashburner et al. 2000; Gene Ontology Consortium 2021) database and filtered for those with supporting biological data. For each term, we summed the $r_{sen,true}$ values across all genes of the term, yielding $s_{sen,true}$. To assess the enrichment for high or low values of this sum, we first took the absolute value, $|s_{sen,true}|$. We then sampled, from the total set of genes with expression data, a random set of the same number as that in the true data for the term; we calculated the species difference $r_{sen,rand}$ for each such gene and the

absolute value of the sum over them all, $|s_{sen,rand}|$. We used as a *p*-value the proportion of 10,000 resampled data sets in which $|s_{sen,true}| > |s_{sen,rand}|$.

For analysis of the impact of *Usf2* knockdown on expression before or 6 hours, 10 days, or 20 days after irradiation (see below), Gene Ontology enrichment tests were as above except that we took the ratio, for a given gene, between the average expression in purebred *M. musculus* (PWK) cells infected with lentivirus harboring scrambled shRNA and the analogous quantity across both *Usf2*-targeting shRNA treatments.

Proteomic analysis of secreted proteins

Conditioned medium preparation. For a given replicate culture, either before irradiation or 10 days after irradiation (see above), cells were washed three times with PBS and incubated with serum and phenol red free DMEM containing 1% pen-strep for 24 hours. The following day the conditioned medium was collected and passed through a 0.45 µm filter to remove cellular debris. The conditioned medium was placed in a -80°C freezer for storage before use as input into proteomic profiling (see below). For proteomic profiles of purebred cells, we carried out this procedure for three technical replicate cultures of one biological replicate per species.

Sample concentration. 30 mL of conditioned media for each replicate were concentrated to 400 µL with 15 mL 3 kDa filters (Millipore Sigma, Burlington, MA). Protein concentration was determined using the Bicinchoninic Acid (BCA) assay (Thermo Fisher Scientific, Waltham, MA).

Protein digestion and desalting. Aliquots of 200 µg protein lysates for each sample were brought to the same overall volume of 52 µL with water, reduced using 20 mM dithiothreitol in 50 mM triethylammonium bicarbonate buffer (TEAB) at 50°C for 10 min, cooled to room

temperature (RT) and held at RT for 10 min, and alkylated using 40 mM iodoacetamide in 50 mM TEAB at RT in the dark for 30 min. Samples were acidified with 12% phosphoric acid to obtain a final concentration of 1.2% phosphoric acid. S-Trap buffer consisting of 90% methanol in 100 mM TEAB at pH ~7.1, was added and samples were loaded onto the S-Trap mini spin columns. The entire sample volume was spun through the S-Trap mini spin columns at 4,000 x g and RT, binding the proteins to the mini spin columns. Subsequently, S-Trap mini spin columns were washed twice with S-Trap buffer at 4,000 x g at RT and placed into clean elution tubes. Samples were incubated for one hour at 47ºC with sequencing grade trypsin (Promega, San Luis Obispo, CA) dissolved in 50 mM TEAB at a 1:25 (w/w) enzyme:protein ratio. Afterwards, trypsin solution was added again at the same ratio, and proteins were digested overnight at 37ºC.

Peptides were sequentially eluted from mini S-Trap spin columns with 50 mM TEAB, 0.5% formic acid (FA) in water, and 50% acetonitrile (ACN) in 0.5% FA. After centrifugal evaporation, samples were resuspended in 0.2% FA in water and desalted with Oasis 10 mg Sorbent Cartridges (Waters, Milford, MA). The desalted elutions were then subjected to an additional round of centrifugal evaporation and re-suspended in 0.2% FA in water at a final concentration of 1 µg/µL. Subsequently, 8 µL of each sample were diluted with 2% ACN in 0.1% FA to obtain a concentration of 400 ng/µL. Finally, 1 µL of indexed Retention Time Standard (iRT, Biognosys, Schlieren, Switzerland) was added to each sample, thus bringing up the total volume to 20 µL (Escher et al. 2012).

Mass spectrometric analysis. Reverse-phase HPLC-MS/MS analyses were performed on a Dionex UltiMate 3000 system coupled online to an Orbitrap Exploris 480 mass spectrometer (Thermo Fisher Scientific, Bremen, Germany). The solvent system consisted of 2% ACN, 0.1% FA in water (solvent A) and 80% ACN, 0.1% FA in ACN (solvent B). Digested peptides (400 ng)

were loaded onto an Acclaim PepMap 100 C_{18} trap column (0.1 x 20 mm, 5 µm particle size; Thermo Fisher Scientific) over 5 min at 5 µL/min with 100% solvent A. Peptides (400 ng) were eluted on an Acclaim PepMap 100 C_{18} analytical column (75 µm x 50 cm, 3 µm particle size; Thermo Fisher Scientific) at 300 nL/min using the following gradient: linear from 2.5% to 24.5% of solvent B in 125 min, linear from 24.5% to 39.2% of solvent B in 40 min, up to 98% of solvent B in 1 min, and back to 2.5% of solvent B in 1 min. The column was re-equilibrated for 30 min with 2.5% of solvent B, and the total gradient length was 210 min. Each sample was acquired in data-independent acquisition (DIA) mode (Gillet et al. 2012; Bruderer et al. 2017; Collins et al. 2017), in triplicates. Full MS spectra were collected at 120,000 resolution (Automatic Gain Control (AGC) target: 3e6 ions, maximum injection time: 60 ms, 350-1,650 *m/z*), and MS2 spectra at 30,000 resolution (AGC target: 3e6 ions, maximum injection time: Auto, Normalized Collision Energy (NCE): 30, fixed first mass 200 *m/z*). The isolation scheme consisted of 26 variable windows covering the 350-1,650 *m/z* range with an overlap of 1 *m/z* (Bruderer et al. 2017).

DIA data processing and statistical analysis. DIA data was processed in Spectronaut (version 15.6.211220.50606) using directDIA. Data extraction parameters were set as dynamic and non-linear iRT calibration with precision iRT was selected. Data was searched against the *Mus musculus* reference proteome with 58,430 entries (UniProtKB-TrEMBL), accessed on 01/31/2018. Trypsin/P was set as the digestion enzyme and two missed cleavages were allowed. Cysteine carbamidomethylation was set as a fixed modification; methionine oxidation and protein N-terminus acetylation were set as dynamic modifications. Identification was performed using 1% precursor and protein q-value. Quantification was based on the peak areas of extracted ion chromatograms (XICs) of 3 – 6 MS2 fragment ions, specifically b- and y-ions, with local normalization and q-value sparse data filtering applied (Supplemental Table S4). In addition, iRT profiling was selected. Senescence specific differential protein secretion

analysis comparing samples derived from unirradiated and senescent *M. musculus* and *M. spretus* cells was performed using the proteomics data as input for a two-factor ANOVA with Benjamini-Hochberg multiple testing correction (Benjamini and Hochberg 1995). Only those proteins with a corrected *p*-value < 0.05 were considered significantly differentially secreted between the species during senescence.

Transcriptomic screen for senescence regulators

To associate expression variation in genes with sequence variation in their upstream binding sites for a given transcription factor, we proceeded as follows. From RNA-seq profiling of *M. musculus* x *M. spretus* F1 hybrid cells (see above), we used the TPM counts for each parent species' allele from each replicate profile from control and senescent conditions as input into a two-factor ANOVA. A given gene was categorized as exhibiting senescence-associated differential allele specific expression if the interaction F statistic value from this ANOVA was among the top 25% of all genes tested. Separately, we used compiled data from chromatin immunoprecipitation via high-throughput sequencing from the Gene Transcription Regulation Database (GTRD) (Yevshin et al. 2019) to identify all experimentally determined transcription factor (TF) binding sites located within a 5kb window upstream of the transcriptional start site for each gene in turn in the *M. musculus* genome; we refer to the downstream gene of each such binding location as the target of the TF. This calculation used *M. musculus* gene start sites from the Ensembl GRCm38.96 GFF. Next, for each binding site, we used the VCF between PWK and STF pseudogenomes (see above) to identify single nucleotide variants between PWK and STF in the binding site locus. Now, for all the target genes of a given TF, we categorized them as having sequence variants or not in the respective binding site, and exhibiting senescence-associated differential allele-specific expression. We eliminated from further consideration any TF with fewer than 250 target genes in each of the four categories. For all remaining TFs, the 2

x 2 contingency table was used as input into a Fisher's exact test with Benjamini-Hochberg multiple testing correction.

Usf2 shRNA vector design, construction and application

Usf2 knockdown shRNA sequences were obtained from the Broad Institute Genetic Perturbation Portal (https://portals.broadinstitute.org/gpp/public/). Two shRNA sequences for *Usf2* (CCGGGCAAGACAGGAGCAAGTAAAGCTCGAGCTTTACTTGCTCCTGTCTTGCTTTTTTGAAT; CCGGACAAGGAGACATAATGCATTTCTCGAG-AAATGCATTATGTCTCCTTGTTTTTTTGAAT), and, separately, a scrambled control sequence (CCTAAGGTTAAGTCGCCCTCGCTCGAGCGAGGGCGACTTAACCTTAGG, Addgene cat. #1864), were each cloned into pLKO.1 puro lentiviral vectors (Addgene cat. #8453). Lentiviral particles containing each of the shRNA constructs were generated by calcium phosphate co-transfection of HEK 293T cells with the shRNA pLKO.1 puro vectors and separate pMDLg/pRRE packaging and pCMV-VSV-G envelope plasmids generously provided by Dr. Marius Walter of the Verdin Lab at the Buck Institute. The number of viral particles generated was determined using the Origene One-Wash™ Lentivirus Titer Kit, p24 ELISA (cat. #TR30038). These particles were used to infect two biological replicates of purebred *M. musculus* (PWK) primary tail fibroblasts at a multiplicity of infection of 5 with 4 µg/mL of polybrene, and infected cells were selected by incubating with 2 µg/mL puromycin for 10 days, changing media and antibiotic every other day. Knockdown of *Usf2* was determined by qPCR, using *Usf2* qPCR primer sequences chosen through NCBI Primer Blast, filtering for those spanning an exon-exon junction. The primer pair with the same efficiency (calculated as $10^{(-1/slope)}$ when plotting log concentration of template cDNA versus Ct) as the internal control *Actb* qPCR primers was chosen: *Usf2* forward 5' TTCGGCGACCACAATATCCAG 3', *Usf2* reverse 5'

TTCGGCGACCACAATATCCAG 3', *Actb* forward 5' CAACCGTGAAAAGATGACCC 3', *Actb* reverse 5' GTAGATGGGCACAGTGTGGG 3'. *Usf2* expression was calculated using the Delta-Delta Ct method (Livak and Schmittgen 2001).

Cell proliferation and DNA damage assays

For each of two biological replicates of purebred *M. musculus* (PWK) cells infected with lentivirus harboring the scrambled control and two of each *Usf2* knockdown, either before irradiation or 6 hours after irradiation (see above), we measured cell proliferation and DNA damage response as follows.

For a given replicate, DNA synthesis was measured via 5-ethynyl-2´-deoxyuridine (EdU) incorporation assays using the Invitrogen™ Click-iT™ Edu Alexa Fluor™ 488 Flow Cytometry Assay Kit (cat. #C10420). Cells were treated with 5 µM EdU in complete medium and left in the incubator overnight. The following day cells were fixed, permeabilized, and treated with Alexa Fluor™ 488 azide before running through a BD LSRFortessa™ Cell Analyzer to identify the percentage of EdU positive cells.

For a given replicate, we carried out a comet assay to measure levels of DNA double stranded breaks for a given replicate culture as described (Olive and Banáth 2006). Briefly, slides scored with a diamond tipped scribe were dipped in 1% low melting point agarose and left at 4ºC overnight. Cells of all genotypes tested were mixed into 1% low melting point agarose at 2×10^4 cells/ml, spread over the prepared slides and left to solidify for 1 hour. Slides were then incubated at 37ºC in 2% sarkosyl, 0.5 M NA_2EDTA and 0.5 mg/mL proteinase K pH 8 lysis buffer overnight. The following day the slides were washed three times in 90 mM Tris, 90 mM boric acid, and 2 mM NA_2EDTA pH 8.5 wash buffer, then subject to electrophoresis at 0.6 V/cm

for 25 minutes in wash buffer. The slides were then washed three times in distilled water and placed in a staining solution containing 5 µg/mL of propidium iodide for 20 minutes. The slides were washed again once with distilled water and multiple representative images were taken of each sample using a Zeiss AxioObserver epi-fluorescent microscope. Images were processed via ZEN Digital Imaging for Light Microscopy (RRID:SCR_013672) and comet tail moments were analyzed via OpenComet (Gyori et al. 2014) in ImageJ (Schneider et al. 2012).

For H2AX assays, for a given replicate, cells were cultured in 8-chamber Nunc™ Lab-Tek™ II Chamber Slides™ (Thermo Fisher cat. # 154453). The day before staining, all cells were seeded at 60-70% confluence in each chamber. Cells were fixed by incubating with 4% paraformaldehyde for 5 minutes at 4ºC and permeabilized using 0.1% Triton X-100 for 15 minutes at room temperature. The cells were then blocked using 3% bovine serum albumin (BSA) in PBS for 45 minutes at room temperature, then incubated with 1 µg/mL of primary antibodies specific to phosphorylated (Ser 139) H2AX (cat. # sc-517348, Santa Cruz Biotechnology) in 3% BSA overnight at 4ºC. The following day the cells were washed in PBS three times before incubating with 2 µg/mL of Alexa 488 secondary antibodies purchased from Invitrogen (cat. # A11001) for two hours at room temperature. Cells were washed three times with PBS then incubated with 0.5 µg/mL DAPI for 5 minutes at room temperature. The cells were washed once more with PBS before mounting for imaging. Multiple representative confocal images of each sample were taken using a Zeiss LSM 710 AxioObserver. Images were processed using ImageJ, taking the average background fluorescence across several nuclei in each field of vision and only counting foci with fluorescence intensities above the background threshold.

In addition to the above, we also carried out EdU incorporation assays on two biological replicates of wild-type primary fibroblasts of the *M. musculus* (PWK) background at five days after irradiation, and observed 0.5 and 1% EdU staining, respectively.

Multivariate ANOVA of irradiation and senescence timecourse

To identify genes whose expression changed in wild-type cells through irradiation and senescence, we used RNA-seq profiling data from purebred *M. musculus* (PWK) cells harboring a scrambled shRNA before and 6 hours, 10 days, and 20 days after irradiation (see Supplemental Tables S1 and S5) as input into a multivariate ANOVA test.

MERLIN regulatory network reconstruction

To reconstruct a regulatory network we used RNA-seq profiling data for purebred *M. musculus* (PWK) cells harboring a scrambled shRNA or a *Usf2*-targeting RNA, before and 6 hours, 10 days and 20 days after irradiation, as input into MERLIN (Roy et al. 2013) with default settings. Analysis used a catalog of murine transcription factors from the Gene Transcription Regulation Database (Yevshin et al. 2019).

Data access

All raw and processed sequencing data generated in this study have been submitted to the NCBI Gene Expression Omnibus (GEO; https://www.ncbi.nlm.nih.gov/geo/) under accession number GSE201217. Raw data and complete MS data sets have been uploaded to the Mass Spectrometry Interactive Virtual Environment (MassIVE) repository, developed by the Center for

Computational Mass Spectrometry at the University of California San Diego, and can be downloaded using the following link: http://massive.ucsd.edu/ProteoSAFe/status.jsp?task=5e7aa6a2b31f4dcfafa679e9d3f3d9c3 (MassIVE ID number: MSV000089246; ProteomeXchange ID: PXD033182). *Enter the username and password in the upper right corner of the page:* Username: MSV000089246_reviewer, Password: winter.

Competing interests

The authors report no competing interests.

Acknowledgements

The authors thank Mary West for support of cell culture resources, Melissa Chao for help with data collection, and Herbert Kasler, Marius Walter, and Eric Verdin for helpful discussions and materials. This work was supported by National Institutes of Health R01 NS116992 and R01 GM120430 to R.B.B and R01 HD094787 to J.M.G. E.E.K.K. was supported by the National Science Foundation Graduate Research Fellowship Program (DGE-1313190). Any opinions, findings, and conclusions or recommendations expressed in this material are those of the author(s) and do not necessarily reflect the views of the National Science Foundation or the National Institutes of Health.

References

Aperlo C, Boulukos KE, Pognonec P. 1996. The basic region/helix-loop-helix/leucine repeat transcription factor USF interferes with Ras transformation. *Eur J Biochem* **241**: 249–253.

Ashburner M, Ball CA, Blake JA, Botstein D, Butler H, Cherry JM, Davis AP, Dolinski K, Dwight SS, Eppig JT, et al. 2000. Gene Ontology: tool for the unification of biology. *Nat Genet* **25**: 25–29.

Baker DJ, Wijshake T, Tchkonia T, LeBrasseur NK, Childs BG, van de Sluis B, Kirkland JL, van Deursen JM. 2011. Clearance of p16Ink4a-positive senescent cells delays ageing-associated disorders. *Nature* **479**: 232–236.

Bakkenist CJ, Drissi R, Wu J, Kastan MB, Dome JS. 2004. Disappearance of the telomere dysfunction-induced stress response in fully senescent cells. *Cancer Res* **64**: 3748–3752.

Bandyopadhyay D, Okan NA, Bales E, Nascimento L, Cole PA, Medrano EE. 2002. Down-regulation of p300/CBP histone acetyltransferase activates a senescence checkpoint in human melanocytes. *Cancer Res* **62**: 6231–6239.

Baron Y, Corre S, Mouchet N, Vaulont S, Prince S, Galibert M-D. 2012. USF-1 Is Critical for Maintaining Genome Integrity in Response to UV-Induced DNA Photolesions. *PLoS Genet* **8**: e1002470.

Basisty N, Kale A, Jeon OH, Kuehnemann C, Payne T, Rao C, Holtz A, Shah S, Sharma V, Ferrucci L, et al. 2020. A proteomic atlas of senescence-associated secretomes for aging biomarker development. *PLOS Biol* **18**: e3000599.

Beauséjour CM, Krtolica A, Galimi F, Narita M, Lowe SW, Yaswen P, Campisi J. 2003. Reversal of human cellular senescence: roles of the p53 and p16 pathways. *EMBO J* **22**: 4212–4222.

Benjamini Y, Hochberg Y. 1995. Controlling the False Discovery Rate: A Practical and Powerful Approach to Multiple Testing. *J R Stat Soc Ser B Methodol* **57**: 289–300.

Blanchet C, Jaubert J, Carniel E, Fayolle C, Milon G, Szatanik M, Panthier J-J, Montagutelli X. 2011. Mus spretus SEG/Pas mice resist virulent Yersinia pestis, under multigenic control. *Genes Immun* **12**: 23–30.

Bouafia A, Corre S, Gilot D, Mouchet N, Prince S, Galibert M-D. 2014. p53 Requires the Stress Sensor USF1 to Direct Appropriate Cell Fate Decision. *PLoS Genet* **10**: e1004309.

Brückmann NH, Bennedsen SN, Duijf PHG, Terp MG, Thomassen M, Larsen M, Pedersen CB, Kruse T, Alcaraz N, Ditzel HJ, et al. 2019. A functional genetic screen identifies the Mediator complex as essential for SSX2-induced senescence. *Cell Death Dis* **10**: 1–12.

Bruderer R, Bernhardt OM, Gandhi T, Xuan Y, Sondermann J, Schmidt M, Gomez-Varela D, Reiter L. 2017. Optimization of Experimental Parameters in Data-Independent Mass Spectrometry Significantly Increases Depth and Reproducibility of Results. *Mol Cell Proteomics MCP* **16**: 2296–2309.

Brunk UT, Terman A. 2002. Lipofuscin: mechanisms of age-related accumulation and influence on cell function. *Free Radic Biol Med* **33**: 611–619.

Campisi J. 2013. Aging, cellular senescence, and cancer. *Annu Rev Physiol* **75**: 685–705.

Campisi J. 2005. Senescent cells, tumor suppression, and organismal aging: good citizens, bad neighbors. *Cell* **120**: 513–522.

Campisi J, Fagagna FDD. 2007. Cellular senescence: when bad things happen to good cells. *Nat Rev Mol Cell Biol*.

Casella G, Munk R, Kim KM, Piao Y, De S, Abdelmohsen K, Gorospe M. 2019. Transcriptome signature of cellular senescence. *Nucleic Acids Res* **47**: 7294–7305.

Chan M, Yuan H, Soifer I, Maile TM, Wang RY, Ireland A, O'Brien JJ, Goudeau J, Chan LJ, Vijay T, et al. 2022. Novel insights from a multiomics dissection of the Hayflick limit. *eLife* **11**. https://doi.org/10.7554/eLife.70283 (Accessed March 10, 2022).

Chen J-H, Ozanne SE. 2006. Deep senescent human fibroblasts show diminished DNA damage foci but retain checkpoint capacity to oxidative stress. *FEBS Lett* **580**: 6669–6673.

Chen N, Szentirmay MN, Pawar SA, Sirito M, Wang J, Wang Z, Zhai Q, Yang H-X, Peehl DM, Ware JL, et al. 2006. Tumor-suppression function of transcription factor USF2 in prostate carcinogenesis. *Oncogene* **25**: 579–587.

Chi TF, Khoder-Agha F, Mennerich D, Kellokumpu S, Miinalainen Ii, Kietzmann T, Dimova EY. 2020. Loss of USF2 promotes proliferation, migration and mitophagy in a redox-dependent manner. *Redox Biol* **37**: 101750.

Childs BG, Baker DJ, Kirkland JL, Campisi J, van Deursen JM. 2014. Senescence and apoptosis: dueling or complementary cell fates? *EMBO Rep* **15**: 1139–1153.

Collins BC, Hunter CL, Liu Y, Schilling B, Rosenberger G, Bader SL, Chan DW, Gibson BW, Gingras A-C, Held JM, et al. 2017. Multi-laboratory assessment of reproducibility, qualitative and quantitative performance of SWATH-mass spectrometry. *Nat Commun* **8**: 291.

Coppé J-P, Desprez P-Y, Krtolica A, Campisi J. 2010a. The senescence-associated secretory phenotype: the dark side of tumor suppression. *Annu Rev Pathol* **5**: 99–118.

Coppé J-P, Patil CK, Rodier F, Krtolica A, Beauséjour CM, Parrinello S, Hodgson JG, Chin K, Desprez P-Y, Campisi J. 2010b. A Human-Like Senescence-Associated Secretory Phenotype Is Conserved in Mouse Cells Dependent on Physiological Oxygen. *PLOS ONE* **5**: e9188.

Coppé J-P, Patil CK, Rodier F, Sun Y, Muñoz DP, Goldstein J, Nelson PS, Desprez P-Y, Campisi J. 2008. Senescence-Associated Secretory Phenotypes Reveal Cell-Nonautonomous Functions of Oncogenic RAS and the p53 Tumor Suppressor. *PLOS Biol* **6**: e301.

Corre S, Galibert M-D. 2005. Upstream stimulating factors: highly versatile stress-responsive transcription factors. *Pigment Cell Res* **18**: 337–348.

Danecek P, Bonfield JK, Liddle J, Marshall J, Ohan V, Pollard MO, Whitwham A, Keane T, McCarthy SA, Davies RM, et al. 2021. Twelve years of SAMtools and BCFtools. *GigaScience* **10**: giab008.

Davalos AR, Coppe J-P, Campisi J, Desprez P-Y. 2010. Senescent cells as a source of inflammatory factors for tumor progression. *Cancer Metastasis Rev* **29**: 273–283.

Dejager L, Libert C, Montagutelli X. 2009. Thirty years of Mus spretus: a promising future. *Trends Genet* **25**: 234–241.

Demaria M, Ohtani N, Youssef SA, Rodier F, Toussaint W, Mitchell JR, Laberge R-M, Vijg J, Van Steeg H, Dollé MET, et al. 2014. An essential role for senescent cells in optimal wound healing through secretion of PDGF-AA. *Dev Cell* **31**: 722–733.

Dimri GP, Lee X, Basile G, Acosta M, Scott G, Roskelley C, Medrano EE, Linskens M, Rubelj I, Pereira-Smith O. 1995. A biomarker that identifies senescent human cells in culture and in aging skin in vivo. *Proc Natl Acad Sci U S A* **92**: 9363–9367.

Dörr JR, Yu Y, Milanovic M, Beuster G, Zasada C, Däbritz JHM, Lisec J, Lenze D, Gerhardt A, Schleicher K, et al. 2013. Synthetic lethal metabolic targeting of cellular senescence in cancer therapy. *Nature* **501**: 421–425.

Escher C, Reiter L, MacLean B, Ossola R, Herzog F, Chilton J, MacCoss MJ, Rinner O. 2012. Using iRT, a normalized retention time for more targeted measurement of peptides. *Proteomics* **12**: 1111–1121.

Fumagalli M, Rossiello F, Mondello C, d'Adda di Fagagna F. 2014. Stable Cellular Senescence Is Associated with Persistent DDR Activation. *PLoS ONE* **9**: e110969.

Gene Ontology Consortium. 2021. The Gene Ontology resource: enriching a GOld mine. *Nucleic Acids Res* **49**: D325–D334.

Gillet LC, Navarro P, Tate S, Röst H, Selevsek N, Reiter L, Bonner R, Aebersold R. 2012. Targeted Data Extraction of the MS/MS Spectra Generated by Data-independent Acquisition: A New Concept for Consistent and Accurate Proteome Analysis*. *Mol Cell Proteomics* **11**: O111.016717.

Gyori BM, Venkatachalam G, Thiagarajan PS, Hsu D, Clement M-V. 2014. OpenComet: An automated tool for comet assay image analysis. *Redox Biol* **2**: 457–465.

Han R, Li L, Ugalde AP, Tal A, Manber Z, Barbera EP, Chiara VD, Elkon R, Agami R. 2018. Functional CRISPR screen identifies AP1-associated enhancer regulating FOXF1 to modulate oncogene-induced senescence. *Genome Biol* **19**: 118.

Hayflick L. 1965. The limited in vitro lifetime of human diploid cell strains. *Exp Cell Res* **37**: 614–636.

Hsu C-H, Altschuler SJ, Wu LF. 2019. Patterns of Early p21 Dynamics Determine Proliferation-Senescence Cell Fate after Chemotherapy. *Cell* **178**: 361-373.e12.

Hu D, Tjon EC, Andersson KM, Molica GM, Pham MC, Healy B, Murugaiyan G, Pochet N, Kuchroo VK, Bokarewa MI, et al. 2020. Aberrant expression of USF2 in refractory rheumatoid arthritis and its regulation of proinflammatory cytokines in Th17 cells. *Proc Natl Acad Sci* **117**: 30639–30648.

Huang R-X, Zhou P-K. 2020. DNA damage response signaling pathways and targets for radiotherapy sensitization in cancer. *Signal Transduct Target Ther* **5**: 1–27.

Kale A, Sharma A, Stolzing A, Desprez P-Y, Campisi J. 2020. Role of immune cells in the removal of deleterious senescent cells. *Immun Ageing* **17**: 16.

Kang C. 2019. Senolytics and Senostatics: A Two-Pronged Approach to Target Cellular Senescence for Delaying Aging and Age-Related Diseases. *Mol Cells* **42**: 821–827.

Khan M, Gasser S. 2016. Generating Primary Fibroblast Cultures from Mouse Ear and Tail Tissues. *J Vis Exp JoVE*. https://www.ncbi.nlm.nih.gov/pmc/articles/PMC4781275/ (Accessed March 23, 2022).

Kim D, Pertea G, Trapnell C, Pimentel H, Kelley R, Salzberg SL. 2013a. TopHat2: accurate alignment of transcriptomes in the presence of insertions, deletions and gene fusions. *Genome Biol* **14**: R36.

Kim E-C, Kim J-R. 2019. Senotherapeutics: emerging strategy for healthy aging and age-related disease. *BMB Rep* **52**: 47–55.

Kim EK, Moon S, Kim DK, Zhang X, Kim J. 2018. CXCL1 induces senescence of cancer-associated fibroblasts via autocrine loops in oral squamous cell carcinoma. *PLOS ONE* **13**: e0188847.

Kim Y-M, Byun H-O, Jee BA, Cho H, Seo Y-H, Kim Y-S, Park MH, Chung H-Y, Woo HG, Yoon G. 2013b. Implications of time-series gene expression profiles of replicative senescence. *Aging Cell* **12**: 622–634.

Krtolica A, Parrinello S, Lockett S, Desprez PY, Campisi J. 2001. Senescent fibroblasts promote epithelial cell growth and tumorigenesis: a link between cancer and aging. *Proc Natl Acad Sci U S A* **98**: 12072–12077.

Kurz DJ, Decary S, Hong Y, Erusalimsky JD. 2000. Senescence-associated (beta)-galactosidase reflects an increase in lysosomal mass during replicative ageing of human endothelial cells. *J Cell Sci* **113 (Pt 20)**: 3613–3622.

Langmead B, Salzberg SL. 2012. Fast gapped-read alignment with Bowtie 2. *Nat Methods* **9**: 357–359.

Lee BY, Han JA, Im JS, Morrone A, Johung K, Goodwin EC, Kleijer WJ, DiMaio D, Hwang ES. 2006. Senescence-associated beta-galactosidase is lysosomal beta-galactosidase. *Aging Cell* **5**: 187–195.

Lee S, Schmitt CA. 2019. The dynamic nature of senescence in cancer. *Nat Cell Biol* **21**: 94–101.

Levi N, Papismadov N, Solomonov I, Sagi I, Krizhanovsky V. 2020. The ECM path of senescence in aging: components and modifiers. *FEBS J* **287**: 2636–2646.

Li H. 2011. A statistical framework for SNP calling, mutation discovery, association mapping and population genetical parameter estimation from sequencing data. *Bioinforma Oxf Engl* **27**: 2987–2993.

Li H, Handsaker B, Wysoker A, Fennell T, Ruan J, Homer N, Marth G, Abecasis G, Durbin R, 1000 Genome Project Data Processing Subgroup. 2009. The Sequence Alignment/Map format and SAMtools. *Bioinforma Oxf Engl* **25**: 2078–2079.

Livak KJ, Schmittgen TD. 2001. Analysis of Relative Gene Expression Data Using Real-Time Quantitative PCR and the 2−ΔΔCT Method. *Methods* **25**: 402–408.

Martínez-Zamudio RI, Roux P-F, de Freitas JANLF, Robinson L, Doré G, Sun B, Belenki D, Milanovic M, Herbig U, Schmitt CA, et al. 2020. AP-1 imprints a reversible transcriptional programme of senescent cells. *Nat Cell Biol* **22**: 842–855.

Nickoloff JA, Boss M-K, Allen CP, LaRue SM. 2017. Translational research in radiation-induced DNA damage signaling and repair. *Transl Cancer Res* **6**: S875–S891.

Olive PL, Banáth JP. 2006. The comet assay: a method to measure DNA damage in individual cells. *Nat Protoc* **1**: 23–29.

Olivieri F, Prattichizzo F, Grillari J, Balistreri CR. 2018. Cellular Senescence and Inflammaging in Age-Related Diseases. *Mediators Inflamm* **2018**: e9076485.

Panneer Selvam S, Roth BM, Nganga R, Kim J, Cooley MA, Helke K, Smith CD, Ogretmen B. 2018. Balance between senescence and apoptosis is regulated by telomere damage-induced association between p16 and caspase-3. *J Biol Chem* **293**: 9784–9800.

Paramos-de-Carvalho D, Jacinto A, Saúde L. 2021. The right time for senescence ed. M.E. Bronner. *eLife* **10**: e72449.

Park JT, Lee Y-S, Cho KA, Park SC. 2018. Adjustment of the lysosomal-mitochondrial axis for control of cellular senescence. *Ageing Res Rev* **47**: 176–182.

Parrinello S, Coppe J-P, Krtolica A, Campisi J. 2005. Stromal-epithelial interactions in aging and cancer: senescent fibroblasts alter epithelial cell differentiation. *J Cell Sci* **118**: 485–496.

Pawar SA, Szentirmay MN, Hermeking H, Sawadogo M. 2004. Evidence for a cancer-specific switch at the CDK4 promoter with loss of control by both USF and c-Myc. *Oncogene* **23**: 6125–6135.

Pérez del Villar L, Vicente B, Galindo-Villardón P, Castellanos A, Pérez-Losada J, Muro A. 2013. Schistosoma mansoni experimental infection in Mus spretus (SPRET/EiJ strain) mice. *Parasite* **20**: 27.

Pinheiro I, Dejager L, Petta I, Vandevyver S, Puimège L, Mahieu T, Ballegeer M, Van Hauwermeiren F, Riccardi C, Vuylsteke M, et al. 2013. LPS resistance of SPRET/Ei mice is mediated by Gilz, encoded by the Tsc22d3 gene on the X chromosome. *EMBO Mol Med* **5**: 456–470.

Podhorecka M, Skladanowski A, Bozko P. 2010. H2AX Phosphorylation: Its Role in DNA Damage Response and Cancer Therapy. *J Nucleic Acids* **2010**: 920161.

Purcell M, Kruger A, Tainsky MA. 2014. Gene expression profiling of replicative and induced senescence. *Cell Cycle Georget Tex* **13**: 3927–3937.

Putri GH, Anders S, Pyl PT, Pimanda JE, Zanini F. 2022. Analysing high-throughput sequencing data in Python with HTSeq 2.0. *Bioinformatics* btac166.

Qyang Y, Luo X, Lu T, Ismail PM, Krylov D, Vinson C, Sawadogo M. 1999. Cell-type-dependent activity of the ubiquitous transcription factor USF in cellular proliferation and transcriptional activation. *Mol Cell Biol* **19**: 1508–1517.

Redon CE, Dickey JS, Bonner WM, Sedelnikova OA. 2009. γ-H2AX as a biomarker of DNA damage induced by ionizing radiation in human peripheral blood lymphocytes and artificial skin. *Adv Space Res Off J Comm Space Res COSPAR* **43**: 1171–1178.

Roy S, Lagree S, Hou Z, Thomson JA, Stewart R, Gasch AP. 2013. Integrated Module and Gene-Specific Regulatory Inference Implicates Upstream Signaling Networks. *PLOS Comput Biol* **9**: e1003252.

Ruuth M, Soronen J, Kaiharju E, Merikanto K, Perttilä J, Metso J, Lee-Rueckert M, Taskinen M-R, Kovanen PT, Öörni K, et al. 2018. USF1 deficiency alleviates inflammation, enhances cholesterol efflux and prevents cholesterol accumulation in macrophages. *Lipids Health Dis* **17**: 285.

Salotti J, Johnson PF. 2019. Regulation of senescence and the SASP by the transcription factor C/EBPβ. *Exp Gerontol* **128**: 110752.

Samarakoon R, Overstreet JM, Higgins SP, Higgins PJ. 2012. TGF-β1 → SMAD/p53/USF2 → PAI-1 transcriptional axis in ureteral obstruction-induced renal fibrosis. *Cell Tissue Res* **347**: 117–128.

Santoro A, Spinelli CC, Martucciello S, Nori SL, Capunzo M, Puca AA, Ciaglia E. 2018. Innate immunity and cellular senescence: The good and the bad in the developmental and aged brain. *J Leukoc Biol* **103**: 509–524.

Sato AYS, Antonioli E, Tambellini R, Campos AH. 2011. ID1 inhibits USF2 and blocks TGF-β-induced apoptosis in mesangial cells. *Am J Physiol Renal Physiol* **301**: F1260-1269.

Schneider CA, Rasband WS, Eliceiri KW. 2012. NIH Image to ImageJ: 25 years of image analysis. *Nat Methods* **9**: 671–675.

Shang D, Sun D, Shi C, Xu J, Shen M, Hu X, Liu H, Tu Z. 2020. Activation of epidermal growth factor receptor signaling mediates cellular senescence induced by certain pro-inflammatory cytokines. *Aging Cell* **19**: e13145.

Siddiqui MS, François M, Fenech MF, Leifert WR. 2015. Persistent γH2AX: A promising molecular marker of DNA damage and aging. *Mutat Res Rev Mutat Res* **766**: 1–19.

Silva E, Ideker T. 2019. Transcriptional Responses to DNA Damage. *DNA Repair* **79**: 40–49.

Song X, Zhu M, Li H, Liu B, Yan Z, Wang W, Li H, Sun J, Li S. 2018. USF1 promotes the development of knee osteoarthritis by activating the NF-κB signaling pathway. *Exp Ther Med* **16**: 3518–3524.

Sun W, Hu Y. 2013. eQTL Mapping Using RNA-seq Data. *Stat Biosci* **5**: 198–219.

Tyler EJ, Gutierrez Del Arroyo A, Hughes BK, Wallis R, Garbe JC, Stampfer MR, Koh J, Lowe R, Philpott MP, Bishop CL. 2021. Early growth response 2 (EGR2) is a novel regulator of the senescence programme. *Aging Cell* **20**: e13318.

Vanlaere I, Vanderrijst A, Guénet J-L, De Filette M, Libert C. 2008. Mx1 causes resistance against influenza A viruses in the Mus spretus-derived inbred mouse strain SPRET/Ei. *Cytokine* **42**: 62–70.

Venkata Narayanan I, Paulsen MT, Bedi K, Berg N, Ljungman EA, Francia S, Veloso A, Magnuson B, di Fagagna F d'Adda, Wilson TE, et al. 2017. Transcriptional and post-transcriptional regulation of the ionizing radiation response by ATM and p53. *Sci Rep* **7**: 43598.

Veyrieras J-B, Kudaravalli S, Kim SY, Dermitzakis ET, Gilad Y, Stephens M, Pritchard JK. 2008. High-Resolution Mapping of Expression-QTLs Yields Insight into Human Gene Regulation. *PLOS Genet* **4**: e1000214.

Vicencio JM, Galluzzi L, Tajeddine N, Ortiz C, Criollo A, Tasdemir E, Morselli E, Ben Younes A, Maiuri MC, Lavandero S, et al. 2008. Senescence, apoptosis or autophagy? When a damaged cell must decide its path--a mini-review. *Gerontology* **54**: 92–99.

Villarroel CA, Bastías M, Canessa P, Cubillos FA. 2021. Uncovering Divergence in Gene Expression Regulation in the Adaptation of Yeast to Nitrogen Scarcity. *mSystems* **6**: e0046621.

Wan M, Gray-Gaillard EF, Elisseeff JH. 2021. Cellular senescence in musculoskeletal homeostasis, diseases, and regeneration. *Bone Res* **9**: 1–12.

Wang Y, Sui Y, Lian A, Han X, Liu F, Zuo K, Liu M, Sun W, Wang Z, Liu Z, et al. 2021. PBX1 Attenuates Hair Follicle-Derived Mesenchymal Stem Cell Senescence and Apoptosis by Alleviating Reactive Oxygen Species-Mediated DNA Damage Instead of Enhancing DNA Damage Repair. *Front Cell Dev Biol* **9**: 739868.

Wang Y, Xu Q, Sack L, Kang C, Elledge SJ. 2016. A gain-of-function senescence bypass screen identifies the homeobox transcription factor DLX2 as a regulator of ATM–p53 signaling. *Genes Dev* **30**: 293–306.

Wittkopp PJ, Haerum BK, Clark AG. 2004. Evolutionary changes in cis and trans gene regulation. *Nature* **430**: 85–88.

Xie Q, Peng S, Tao L, Ruan H, Yang Y, Li T-M, Adams U, Meng S, Bi X, Dong M-Q, et al. 2014. E2F Transcription Factor 1 Regulates Cellular and Organismal Senescence by Inhibiting Forkhead Box O Transcription Factors. *J Biol Chem* **289**: 34205–34213.

Yang K, Wang F, Zhang H, Wang X, Chen L, Su X, Wu X, Han Q, Chen Z, Chen Z-S, et al. 2021. Target Inhibition of CBP Induced Cell Senescence in BCR-ABL- T315I Mutant Chronic Myeloid Leukemia. *Front Oncol* **10**. https://www.frontiersin.org/article/10.3389/fonc.2020.588641 (Accessed March 10, 2022).

Yevshin I, Sharipov R, Kolmykov S, Kondrakhin Y, Kolpakov F. 2019. GTRD: a database on gene transcription regulation-2019 update. *Nucleic Acids Res* **47**: D100–D105.

Zhang C, Zhang X, Huang L, Guan Y, Huang X, Tian X-L, Zhang L, Tao W. 2021. ATF3 drives senescence by reconstructing accessible chromatin profiles. *Aging Cell* **20**: e13315.

Zhang X, Li J, Sejas DP, Pang Q. 2005. The ATM/p53/p21 pathway influences cell fate decision between apoptosis and senescence in reoxygenated hematopoietic progenitor cells. *J Biol Chem* **280**: 19635–19640.

Zhao H, Darzynkiewicz Z. 2013. Biomarkers of Cell Senescence Assessed by Imaging Cytometry. *Methods Mol Biol Clifton NJ* **965**: 83–92.

1031